Spin-dependent hybridization of image-potential states and overlayer states: One monolayer of Tl on Ag(111)

Sven Schemmelmann [1,*] Peter Krüger [2] Patrick Härtl [3] and Markus Donath [1,†]

[1]*Physikalisches Institut, Universität Münster, Wilhelm–Klemm–Straße 10, 48149 Münster, Germany*

[2]*Institut für Festkörpertheorie, Universität Münster, Wilhelm–Klemm–Straße 10, 48149 Münster, Germany*

[3]*Physikalisches Institut, Experimentelle Physik II, Julius-Maximilians-Universität Würzburg, Am Hubland, 97074 Würzburg, Germany*

(Received 5 February 2024; revised 11 March 2024; accepted 21 March 2024; published 9 April 2024)

We present a study of the unoccupied electronic states of one monolayer (ML) Tl epitaxially grown on Ag(111) in a moiré superstructure. This two-dimensional atomic-layer material is investigated by scanning tunneling microscopy/spectroscopy, spin-resolved inverse photoemission, and calculations based on density functional theory. The unoccupied band structure exhibits characteristic spin-dependent hybridization between overlayer states influenced by the substrate. Most of the experimentally observed bands, their $E(\mathbf{k}_\parallel)$ behavior, and their Rashba-type spin dependence can be qualitatively described by a simple model for a Tl/Ag bilayer. A more realistic superstructure model reflecting the moiré structure provides deeper insight into the hybridization mechanisms for states of different orbital composition, further elucidated by calculations of the charge densities. Experimentally, $E(\mathbf{k}_\parallel)$ measurements as well as the analysis of spin-dependent spectral intensities allow us to distinguish different orbital contributions in the respective spin-up and spin-down components leading to hybridization gaps with spin-dependent size. Most interestingly, spin-dependent hybridization with overlayer states was discovered for an image-potential-induced surface band, which is mainly located in front of the sample surface.

DOI: 10.1103/PhysRevB.109.165417

I. INTRODUCTION

Two-dimensional atomic-layer materials on solid surfaces play an increasing role in today's research on quantum information devices [1]. Here, the understanding of the electronic states is of vital importance. In particular, phenomena related to the electron spin play an important role for spintronic applications. The research field of spintronics is based on the idea of using the electronic spin as information carrier. In order to obtain spin-polarized electron states, the spin degeneracy of the states must be lifted. This can be achieved either by exchange interaction or spin-orbit coupling (SOC).

SOC leads to various effects in electronic states with the Rashba effect as the most prominent example [2]. It was first observed for the L-gap surface state of Au(111) [3,4]. The effects of SOC can be observed mainly in materials with high atomic number. This makes Tl with an atomic number of $Z = 81$ as one of the heaviest nonradioactive elements an interesting candidate to study. Consequently, interesting effects of SOC have been observed in thin Tl films on various substrates. In Tl/Si(111) and Tl/Ge(111), SOC leads to a giant spin splitting with a rotation of the spin-polarization direction as a function of $\mathbf{k}_\parallel$ [5–9], while an anisotropic peculiar Rashba effect was found on Tl/Si(110) [10]. In a bilayer Tl film grown on Ag(111), the locally broken inversion symmetry leads to spin-polarized bands, in which the spins in each layer are oppositely polarized [11]. In this paper, we investigate effects of SOC in the unoccupied electronic structure of one monolayer (ML) Tl on Ag(111). To some extent, the electron states around $\overline{\Gamma}$ in Tl/Ag(111) [12] are reminiscent of states in the sample system Pb/Cu(111), where spin-dependent hybridization gaps were observed [13]. In the system Tl/Ag(111), we discovered spin-dependent hybridization even between image-potential-induced states and overlayer states.

In general, image-potential states form a two-dimensional electron gas several Å in front of the surface. Their wavefunctions have only minor overlap with states of the the outermost atomic layers [14,15]. Despite this very small overlap, image-potential states can exhibit an exchange splitting on magnetic surfaces [16–18] as well as a Rashba splitting on surfaces with strong spin-orbit interaction [19–21]. However, no spin-dependent hybridization effects of image-potential states have been reported so far in the literature. Yet, the resonant character of the image-potential states in Tl/Ag(111) increases the overlap with other states, which enables hybridization effects in this system.

In this paper, we present scanning tunneling microscopy/spectroscopy data for 1 ML Tl epitaxially grown on Ag(111) and investigate the unoccupied electronic structure by spin- and angle-resolved inverse photoemission (IPE). The experimental results are substantiated by band structure and charge distribution calculations obtained by density functional theory (DFT).

II. EXPERIMENTAL METHODS

All experiments have been performed in an ultrahigh-vacuum apparatus with a base pressure of $<5 \times 10^{-11}$ mbar.

*Corresponding author: sven.schemmelmann@uni-muenster.de

†Corresponding author: markus.donath@uni-muenster.de

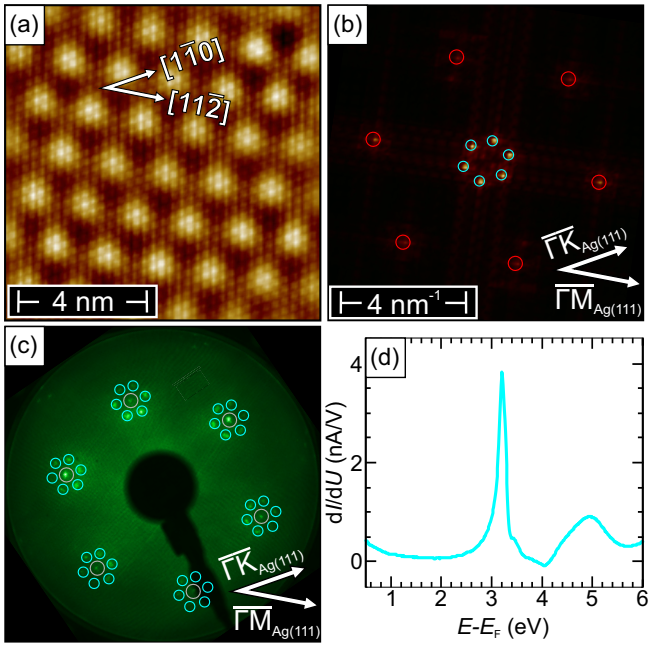

FIG. 1. (a) Atomic resolution STM topography of 1 ML Tl/Ag(111) superimposed by a moiré superstructure. (b) 2D-FFT of (a), with the marked moiré spots in cyan and the Tl spots in red. (c) LEED pattern, where the diffraction spots for Ag and the moiré spots are marked with gray- and cyan-colored circles, respectively. (d) dI/dU-point spectrum taken at a comparable surface as shown in (a) in the energy range of $0.5\,\text{eV} \leqslant E - E_\text{F} \leqslant 6.0\,\text{eV}$. STM parameters: $U_\text{bias} = 10\,\text{mV}$, $I_\text{set} = 25\,\text{nA}$, $T_\text{STM} \approx 5\,\text{K}$. STS parameters: $U_\text{mod} = 10\,\text{mV}$, $I_\text{set} = 1\,\text{nA}$, $\nu = 733$ Hz. LEED parameters: $E_\text{LEED} = 120\,\text{eV}$, $T_\text{LEED} \approx 300\,\text{K}$.

The Ag(111) substrate was cleaned by cycles of Ar ion sputtering at an energy of 600 eV and annealing to ≈700 K. Subsequently, one ML of Tl was deposited by a home-built evaporator, while the substrate was held at a temperature of ≈480 K.

The Tl overlayer forms a moiré superstructure, caused by the lattice mismatch between Tl and Ag, which is checked via scanning tunneling microscopy (STM) topography and low-energy electron diffraction (LEED) measurements. The results are summarized in Fig. 1. The topography in Fig. 1(a) shows the atomically resolved Tl layer, which is superimposed by the much longer modulation of the moiré superstructure. Figure 1(b) illustrates the corresponding two-dimensional fast Fourier transform (2D-FFT) of Fig. 1(a). This figure shows both the hexagonally arranged patches of the Tl layer (red circles) oriented along the $\overline{\Gamma}\,\overline{\text{M}}_{\text{Ag}(111)}$ axes and the moiré superstructure (cyan circles) rotated by ≈24° with respect to the Tl lattice. Here in reciprocal space, the Tl lattice has the larger lattice constant compared to the moiré superstructure. In Fig. 1(c) a LEED diffraction image is shown. In addition to the Ag(111) spots (gray circles), the figure shows the moiré superstructure marked with cyan circles, indicating that the moiré superstructure is rotated by ≈26° with respect to the Ag(111) lattice. The small variation in the rotation angles of the moiré superstructure with respect to the Ag(111) lattice in Figs. 1(b) and 1(c) may be explained by different measuring temperatures of $T_\text{STM} \approx 5$ K and $T_\text{LEED} \approx 300$ K, respectively, which may cause slight temperature-dependent structural modifications. Figure 1(d) shows a dI/dU-point spectrum in the energy range of $0.5\,\text{eV} \leqslant E - E_\text{F} \leqslant 6.0$ eV of the moiré superstructure, with a sharp maximum at $E - E_\text{F} \approx 3.20$ eV, comparable to the data already presented in [12]. The overall growth behavior and analysis of Tl on Ag(111) is described in Ref. [12].

The unoccupied electronic structure was investigated at room temperature by spin- and angle-resolved IPE [22,23]. For excitation with spin-polarized electrons, we used a GaAs-based photocathode as electron source with a spin polarization of 29% [24]. The electron spin polarization is aligned in the surface plane and perpendicular to $\mathbf{k}_\parallel$, i.e., along the Rashba component. The electrons are guided to the sample via an electron optics and impinge on the sample at an angle θ with respect to the surface normal with an angular resolution of $\Delta\theta \approx 3^\circ$ [25]. The emitted photons from transitions into unoccupied electronic states are detected via two bandpass detectors with a mean detection energy of $\hbar\omega = 9.9\,\text{eV}$ [26]. Counter C1 is located at an angle of 65° with respect to the electron beam within the measuring plane and 32° out of it, while counter C2 is located at an angle of −70° within the measuring plane, i.e., on the opposite side of the electron beam (see Fig. 4 below). The sign of θ is defined in such a way that in measurements for negative θ the surface normal is rotated towards C2. The overall energy resolution is about 400 meV [7].

III. THEORETICAL METHODS

We employ density functional theory (DFT) with the local-density approximation (LDA) [27] to obtain the structural and electronic properties of the system. These calculations [28] are performed employing nonlocal norm-conserving pseudopotentials in the separable Kleinman-Bylander form [29] including scalar-relativistic corrections and spin-orbit coupling (SOC) [30]. Electronic wavefunctions are represented by Gaussian orbitals with s, p, and d symmetries.

Calculations have been conducted for two model systems. In a first simple model, the electronic structure of a bilayer containing one ML Tl and one ML Ag is calculated. The Ag layer is saturated by H atoms to suppress the interaction with the retral Ag surface state [31]. Thereby, Tl and Ag have the same in-plane nearest-neighbour (NN) distance of 3.48 Å, which represents the experimental NN distance of the Tl monolayer. The Tl atoms are positioned on the threefold hollow sites of the Ag layers.

In a second more realistic model, the moiré structure is treated by a supercell with a large lateral lattice constant. To take the mismatch between the Ag and the Tl lattice into account, a (4×4) cell of Tl corresponding to a (5×5) cell of reconstructed Ag is employed. Using the experimental NN distance of 3.48 Å for the Tl adlayer, neighboring Ag atoms have in average a distance of 2.78 Å in each layer. This is slightly smaller than the NN distance of 2.86 Å in bulk silver. The supercell contains a Tl layer, five Ag layers and a saturating layer of H atoms to inhibit the interaction between top and bottom surface states. Relaxations on the topmost four layers

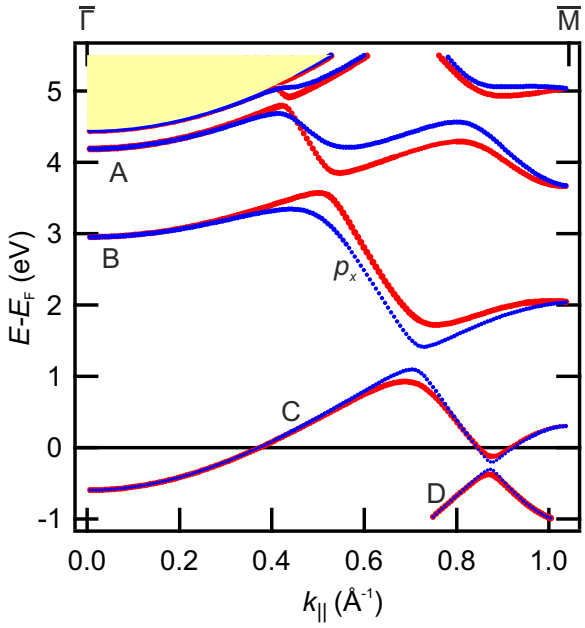

FIG. 2. Calculated band structure of a Tl/Ag bilayer in a (1×1) unit cell. The red (blue) dot size indicates the Rashba component of the spin-expectation value for spin-up (spin-down) electrons. The light-yellow area represents the region of vacuum continuum states.

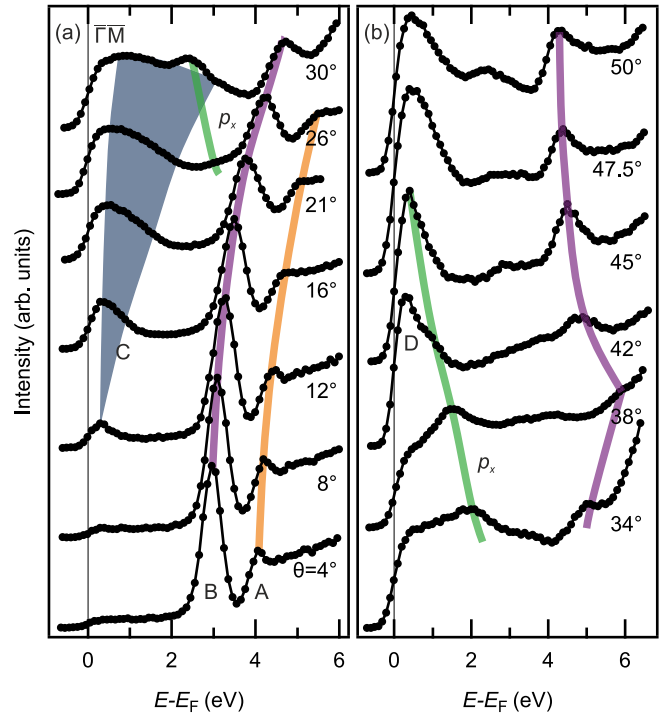

FIG. 3. Spin-integrated IPE spectra of Tl/Ag(111) for various angles of electron incidence θ. The dispersions of selected spectral features are highlighted by colored lines.

were taken into account. The resulting NN distances between Tl and Ag atoms are between 2.94 Å and 3.26 Å.

Since the LDA does not lead to an image-like surface barrier, we replace in both models the LDA potential in the vacuum region by a potential [32] containing the correct $1/z$ asymptotic tail. To represent the wavefunctions in the vacuum, Gaussian orbitals located at the positions of the missing Tl atoms are used.

We simulate the inverse-photoemission process by assuming a plane wave as the initial state and compute the dipole transition matrix elements employing the final states resulting from our DFT calculations. An exponential damping term with a decay length of 1.25 Å has been used to consider the finite penetration depth of the incoming electrons.

IV. RESULTS AND DISCUSSION

A. Expectations from the bilayer model

We start our analysis with a look at the theoretical electronic structure of our bilayer model system of 1 ML Tl/1 ML Ag. The resulting band structure along the $\overline{\Gamma}\,\overline{\mathrm{M}}$ direction (which we define as x direction) is shown in Fig. 2, where four parabolically dispersing states are visible. The state labeled A at about $E - E_F = 4.2$ eV at $\overline{\Gamma}$ is an image-potential state, while state B at about 3 eV is derived from s, p_z, and d_{z^2} states of the Tl monolayer coupled to the Ag substrate (s, d_{z^2}). The third state C at about 0.5 eV below E_F is a result of a Tl p_z state of the free standing monolayer coupled to Ag p_z and d_{z^2} states. The state labeled D below the Fermi energy originates from Tl p_z states coupled to s and d_{xz} states of Ag. Additionally, we find a state with downward energy dispersion crossing the dispersion of the aforementioned states. This state is a Tl p_x state that hybridizes with the other states. As a result, spin-dependent hybridization gaps open at the crossing points. In particular, for state B, the hybridization is strongly spin dependent resulting in a large hybridization gap for spin down and a small one for spin up. This scenario is strongly reminiscent of the behavior of an overlayer band in Pb/Cu(111) [13]. The hybridization of p_x with C opens a hybridization gap with opposite spin dependence (small for spin down, large for spin up). Changing the positions of the Tl atoms in the simple model from hollow to top or bridge sites, however, changes the spin splitting for C, i.e., spin up has a smaller hybridization gap than spin down (not shown) [33]. Therefore, we expect a more complex behavior in experiment, since the real sample system can be considered as a superposition of all atomic positions.

Interestingly, the calculation predicts hybridization between the image-potential state A and the Tl p_x state. This may come as a surprise, since image-potential states exist far in front of the surface with only small overlap with electronic states of the sample. Therefore, in our data analysis, we will pay special attention to whether such hybridization effects can be observed experimentally. We note that, as in the case of C, the spin structure is influenced by the particular atomic positions within the model.

B. Experimental results

Figure 3 presents spin-integrated IPE spectra for various angles of incidence θ. The energy dispersions of the prominent spectral features are highlighted by colored lines. For small θ, two features stand out with an upward energy dispersion for increasing θ, marked by orange and purple lines.

Their energy positions and parabolic dispersion in comparison with the model calculation in Fig. 2 suggest that these states represent the predicted states A and B. The spectral shape of A, a peak followed by a step-like increase of the background, is characteristic of an image-potential state [34]. Furthermore, the energy of B around normal incidence coincides with our STS measurement in Fig. 1(d). The dispersion, effective mass, and spin dependence of A and B was already discussed in our previous publication [12]. Experimentally, we obtained effective masses for A and B of $m_A^*/m_e = 1.2 \pm 0.1$ and $m_B^*/m_e = 1.6 \pm 0.2$, respectively. The effective mass for A is very similar to values of about 1.3 for the $n = 1$ image-potential state of the pristine Ag(111) surface [35,36]. For small angles, the states A and B exhibit no spin splittings. With the measured work function of $\phi = 4.3$ eV, the binding energy of the image-potential state A amounts to 0.3 eV with respect to vacuum level, which is small compared with typical binding energies (0.85 eV to 0.38 eV) of image states within a bandgap [14,15]. This suggests that A is an image-potential resonance rather than an image-potential state. The downward dispersing state between 4 eV and 5 eV for angles higher than $\theta = 40^\circ$ is attributed to state B in the second Brillouin zone of the (1×1) Tl adlayer.

In the spectrum for $\theta = 12^\circ$, a further spectral feature C appears above the Fermi energy. With increasing θ, this feature broadens and gains intensity. It may be associated with state C of the model calculation. However, the broad linewidth of several eV, indicated by the gray-shaded area, questions this interpretation. It seems that this feature comprises several states, which are not represented in the simple model. In the spectrum for $\theta = 26^\circ$, an additional feature is starting to split off from B. This feature disperses downwards and is, therefore, identified as the p_x state of Tl (marked with a green line in Fig. 3). The high spectral intensity just above the Fermi level for $\theta \geqslant 42^\circ$ is associated with state D in the model calculation.

The experimentally obtained angular dependence of the spectral features is qualitatively well described by the band structure of the simple model in Fig. 2. Additionally, the spectra for angles up to 26° are reminiscent of the spectra obtained for Pb/Cu(111) [13]. In this sample system, hybridization of a p_z-like Pb-Cu state and a p_x-like Pb state was observed. In particular, the spin-resolved spectra revealed spin-dependent hybridization gaps in a similar way as it is predicted for Tl/Ag(111) by our model calculation.

To check whether similar spin-dependent hybridization effects occur for Tl/Ag(111), we have taken spin-resolved IPE spectra in small angular steps. They are displayed in Fig. 4 for positive angles between $\theta = 18^\circ$ and 26° in (a), for negative angles between $\theta = -18^\circ$ and -24° in (b), and for larger positive angles between $\theta = 28^\circ$ and 42° in (c). Spectra for positive θ were measured with counter C1, while C2 was used for spectra with negative θ. The spectra show a distinct spin dependence, which changes sign upon changing the sign of θ as expected for a spin-orbit-induced Rashba-type behavior. Small deviations from a perfect reversal of the spin dependence are expected because the photon detection geometries of C1 and C2 are slightly different.

For $\theta = 18^\circ$, A and B show almost no spin-dependent energy splitting, only B shows spin-dependent intensities. This

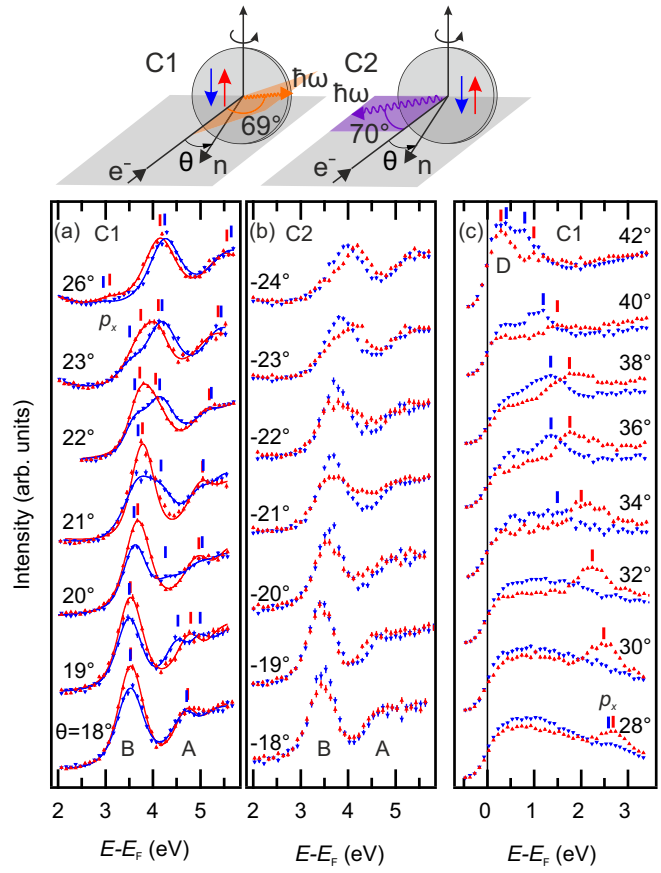

FIG. 4. Spin-resolved IPE spectra for positive (a) and negative (b) angles of incidence θ between 18° and 26° showing clear evidence of reversed spin asymmetry upon sign reversal of the momentum. Spectra for higher positive angles are shown in (c). Peak positions for spin down (blue) and spin up (red) are indicated by tickmarks [37]. Spectra for positive (negative) angles of incidence were measured with counter C1 (C2). The experimental geometries are sketched on top of the (a) and (b) columns.

changes with increasing θ. A small spin splitting is observed for B and, more remarkably, an almost pure spin-down state splits off from the image-potential state A with downward dispersion and merges into B. In addition, B splits into two states, one following the parabolic dispersion and the other disperses downwards in energy while losing intensity. From our theoretical model, we identify the downward dispersing feature as the p_x-type band of Tl. For $\theta = 26^\circ$, the p_x-derived feature at $E - E_F \approx 3$ eV has only small intensity but gains intensity especially in its spin-up part for higher angles. From $\theta = 28^\circ$ to 32°, the state has almost pure spin-up intensity but between $\theta = 34^\circ$ and 38° this state has similar intensities in both spin channels, now with a clear energy splitting. For even higher θ, the spin-down feature gains again intensity while the state crosses the dispersion of state D that appears above E_F at about $\theta = 42^\circ$.

C. Discussion based on the moiré superstructure model

The experimental results are summarized in an $E(\mathbf{k}_\parallel)$ diagram shown in Fig. 5(a), which underlines the parabolic dispersion of the states A and B with effective masses of 1.2

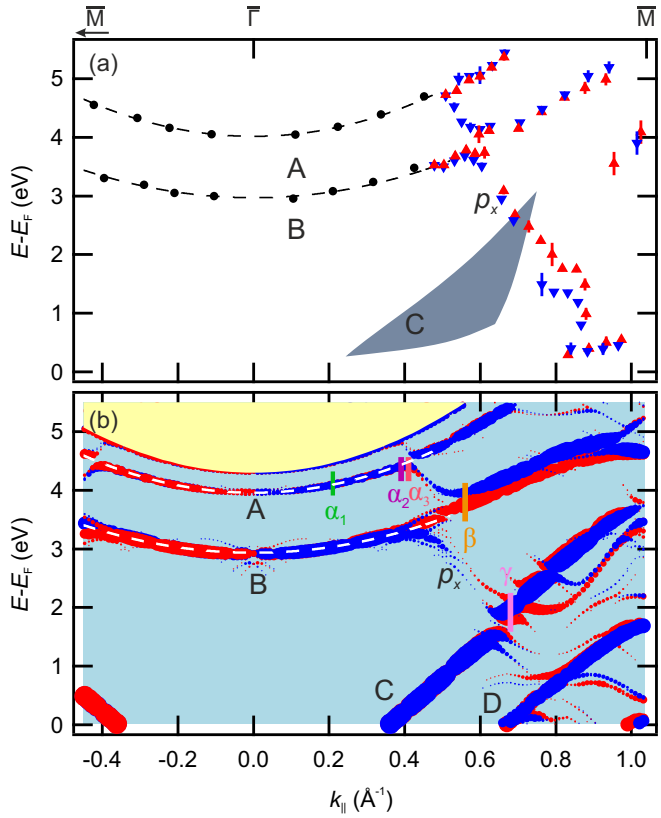

FIG. 5. (a) $E(\mathbf{k}_\parallel)$ dispersion of the spectral features marked in Figs. 3 and 4. Blue symbols are used for spin-down, red for spin-up, and black for spin-integrated spectral features. (b) Calculated photocurrent for the moiré superstructure model. The light-yellow area resembles the region of vacuum continuum states and the light blue area indicates regions of backfolded Ag bulk bands. The dot size represents the intensity of the spin-dependent calculated photocurrent. The markers α_i, β, and γ indicate **k** points, at which the charge distribution was calculated for the states A, B, and C, respectively (see Figs. 6 and 7). The black [in (a)] and white [in (b)] dashed lines indicate parabolic dispersions of A and B with effective masses m^*/m_e of 1.2 and 1.6, respectively.

and 1.6, respectively, as indicated by dashed lines. Additionally, a spin-dependent hybridization gap between B and the downward dispersing p_x state opens in the crossing region. The gap is rather large for spin down and much smaller for spin up as expected from the calculations in Fig. 2. The gray-shaded area in Fig. 5(a) represents the gray-shaded area of Fig. 3, where the state C is observed. The hybridization of the downward dispersing Tl p_x state with the other states A, C, and D, which is also expected from Fig. 2, is hardly visible in the data.

To gain more insight into the spin-dependent hybridization scenarios of the system 1 ML of Tl on Ag(111), we use the results of our more advanced model described in Sec. III. For the large (4×4) unit cell of this system, backfolding leads to a large number of bands throughout the Brillouin zone, which complicates the analysis of the electronic structure. The blue-shaded area in Fig. 5(b) indicates regions of backfolded Ag bulk bands. To enable a direct comparison between theory and experiment, we calculated the photocurrent (see Sec. III). The results, which are presented in Fig. 5(b), unveil the dispersion of the adsorbate-induced electronic states, how they can be expected in our IPE spectra. The overall $E(\mathbf{k}_\parallel)$ dependence of the photocurrent is very similar to the bands of the simple model as shown in Fig. 2 except for the exact energetic positions. Similar to the simple model, four parabolically dispersing states A to D are visible together with a downward dispersing Tl p_x state. In particular, the parabolic dispersion of A and B around $\overline{\Gamma}$ resembles well the experimental results [see black and white dashed lines in Figs. 5(a) and 5(b)]. The Tl p_x state hybridizes with all states in the crossing regions leading to spin-dependent hybridization gaps. The situation is most clear for state B, where a hybridization gap of several hundreds of meV opens for spin down, while it almost vanishes for spin up. This behavior is well confirmed by our IPE results. A very similar behavior was identified and explained in detail for Pb/Cu(111) [13]. The other hybridization gaps are less pronounced and their spin dependence less clear, again in line with our $E(\mathbf{k}_\parallel)$ data.

However, there is more experimental information available than the energy position of a spectral feature: the spectral intensity. In cases, where the orbital composition of the state is independent of its spin character, the intensities in both spin channels are expected to be comparable. In cases, where spin-up and spin-down band components have different orbital symmetries, e.g., caused by hybridization, the spectral intensities for spin up and spin down might differ. As a consequence, far away from a hybridization point, the downward dispersing p_x state should have the same orbital character for spin-up and spin-down electrons leading to the same spectral intensities for both spin states. In contrast, the considerable higher spin-up intensities for p_x in the spectra between $\theta = 28^\circ$ and 34° indicate significant hybridization with state C. This conclusion is further supported by the fact that the p_x state is located within the gray-shaded area of C in Figs. 3 and 5(a). Similarly, the high intensity for spin down in the spectra for $\theta = 40^\circ$ and 42° at about $E - E_F = 1$ eV also indicates hybridization of the p_x state with D.

D. Spin-dependent hybridization of image-potential state

Less expected and, therefore, most interestingly, our calculations predict hybridization of the Tl p_x state with the image-potential-induced surface state A. Image-potential states exist several Å in front of a surface and their wave functions exhibit only minor overlap with electronic states of the outermost layers. The calculated hybridization gap visible in Fig. 5(b) between A and p_x is, however, too small be be observed as an energy gap in our IPE. Nevertheless, with the same argument used for C and D, we searched for indications of hybridization between A and p_x via analyzing spin-resolved IPE spectral intensities. In the spectra for $\theta = 19^\circ$ to 21°, a significant spin-down intensity splits off the image-state emission and disperses downward in energy, well above the hybridization crossing between B and p_x. This striking behavior, also observed with opposite spin order in the spectra for negative θ, is a clear fingerprint of hybridization between the image-potential state A and p_x. If the downward dispersing feature were caused by the p_x state alone, spin-down and spin-up intensities would be comparable.

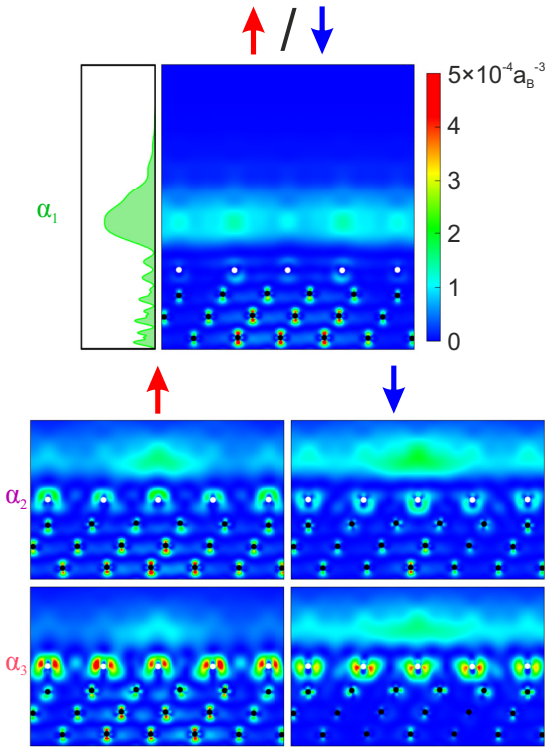

FIG. 6. Charge distribution of the image-potential-induced state A in the xz plane containing Tl as well as Ag atoms for different $\mathbf{k}_\parallel$ points as indicated in Fig. 5. At α_1, the charge distribution is identical for both spin directions, while it is different for the two spin directions at α_2 and α_3. The white (black) dots represent the positions of Tl (Ag) atoms. The layer-dependent charge density at α_1 is presented on the left-hand side of the upper diagram.

Besides the experimental evidence of hybridization between image-potential states and Tl p_x states in the atomic-layer material Tl on Ag(111), we tested our findings by calculations of the charge distribution of the respective states at selected $\mathbf{k}_\parallel$ points: α_1, α_2, and α_3, as indicated in Fig. 5(b). The charge distributions are presented in Fig. 6. At $\alpha_1 = 0.21\,\text{Å}^{-1}$, which is far away from the hybridization point, the charge distribution is predominantly concentrated in front of the surface for both spin components. This is a typical fingerprint of a surface state caused by the image potential. However, the substantial charge distribution within the first atomic layers indicates the surface-resonant character of A, as already proposed in Ref. [12], which enables hybridization with states of proper symmetry at the sample surface.

The charge distributions at $\alpha_2 = 0.39\,\text{Å}^{-1}$ and $\alpha_3 = 0.41\,\text{Å}^{-1}$ show a significant dependence on $\mathbf{k}_\parallel$ and spin. This in turn is a proof of hybridization. At α_2, the states are mainly image-potential like with only a small admixture of Tl p_x orbitals. At α_3, which is even closer to the hybridization point, the charge distribution in front of the surface is strongly reduced for both spin components and the Tl p_x contribution is distinctly increased. Furthermore, these hybridization effects are stronger for the energetically lower lying spin-up states (red) compared with the spin-down states (blue), leading to different experimental intensities for the different spin states.

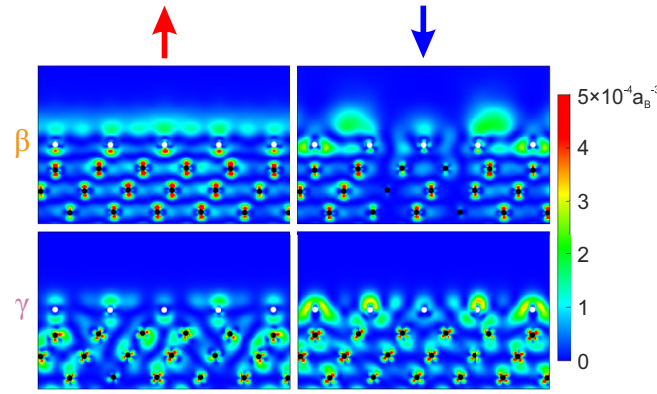

FIG. 7. Charge distribution for states B and C. For both states, the selected $\mathbf{k}_\parallel$ points β and γ [as indicated in Fig. 5(b)] are at higher $\mathbf{k}_\parallel$ than the respective hybridization points. The white (black) dots represent the positions of Tl (Ag) atoms.

A similar behavior of the charge distributions was observed for the spin-dependent hybridization scenarios of B and C, as shown in Fig. 7. At $\beta = 0.56\,\text{Å}^{-1}$ [see Fig. 5(b)], the charge distribution of B reveals that the spin-up part keeps its s, p_z, and d_{z^2} character. For the spin-down state, however, a strong admixture of Tl p_x orbitals is obtained. Strong hybridization leads to a large hybridization gap for spin-down states. Almost vanishing hybridization for spin-up states results in the small hybridization gap. For state C at $\gamma = 0.68\,\text{Å}^{-1}$, we find the same behavior with a small hybridization gap for spin-up states, which keep their Tl p_z character coupled to p_z and d_{z^2} states of the substrate. In contrast, the spin-down states hybridize strongly with Tl p_x states resulting in spin-dependent intensities as observed in experiment.

V. CONCLUSION

We investigated the two-dimensional atomic-layer material Tl/Ag(111) with emphasis on the unoccupied electronic structure by scanning tunneling microscopy/spectroscopy, spin-resolved inverse photoemission and DFT-based calculations. The latter were performed for a simple Tl/Ag bilayer system and a more realistic superstructure model to reflect the experimentally observed moiré structure. The unoccupied band structure shows characteristic spin-dependent hybridization between overlayer and substrate states. Most of the experimentally observed bands can be qualitatively described by the simple model, not only with respect to their $E(\mathbf{k}_\parallel)$ behavior but also their Rashba-type spin dependence. Details of the hybridization mechanism are revealed by superstructure model calculations for the band structure as well as their charge distributions at specific $\mathbf{k}_\parallel$ points. Experimentally, we used not only $E(\mathbf{k}_\parallel)$ measurements but also the analysis of spin-dependent spectral intensities to distinguish different orbital contributions in the respective spin-up and spin-down components. We observed a similar behavior for all investigated hybridizations: strong hybridization in one spin state and almost vanishing hybridization in the other spin state leads to spin-dependent hybridization gaps. Most interestingly, this

behavior was also observed for an image-potential-induced surface band, which is mainly located in front of the sample surface.

ACKNOWLEDGMENT

The authors thank Th. J. Welling for his help with the sample preparation.

[1] K. Sakamoto, T. Kobayashi, K. Yaji, T. Shishidou, and M. Donath, Spin-polarized electrons in atomic layer materials formed on solid surfaces, Prog. Surf. Sci. **97**, 100665 (2022).

[2] Y. A. Bychkov and E. I. Rashba, Properties of a 2D electron-gas with lifted spectral degeneracy, Pis'ma Zh. Eksp. Teor. Fiz. **39**, 66 (1984) [JETP Lett. **39**, 78 (1984)].

[3] S. LaShell, B. A. McDougall, and E. Jensen, Spin splitting of an Au(111) surface state band observed with angle resolved photoelectron spectroscopy, Phys. Rev. Lett. **77**, 3419 (1996).

[4] G. Nicolay, F. Reinert, S. Hüfner, and P. Blaha, Spin-orbit splitting of the L-gap surface state on Au(111) and Ag(111), Phys. Rev. B **65**, 033407 (2001).

[5] J. Ibañez-Azpiroz, A. Eiguren, and A. Bergara, Relativistic effects and fully spin-polarized Fermi surface at the Tl/Si(111) surface, Phys. Rev. B **84**, 125435 (2011).

[6] S. D. Stolwijk, A. B. Schmidt, M. Donath, K. Sakamoto, and P. Krüger, Rotating spin and giant splitting: unoccupied surface electronic structure of Tl/Si(111), Phys. Rev. Lett. **111**, 176402 (2013).

[7] S. D. Stolwijk, K. Sakamoto, A. B. Schmidt, P. Krüger, and M. Donath, Thin line of a Rashba-type spin texture: Unoccupied surface resonance of Tl/Si(111) along $\overline{\Gamma}\,\overline{M}$, Phys. Rev. B **90**, 161109(R) (2014).

[8] S. D. Stolwijk, K. Sakamoto, A. B. Schmidt, P. Krüger, and M. Donath, Spin texture with a twist in momentum space for Tl/Si(111), Phys. Rev. B **91**, 245420 (2015).

[9] P. Eickholt, P. Krüger, S. D. Stolwijk, A. B. Schmidt, and M. Donath, Effects of orbital composition in a pair of spin-orbit-split surface bands at Tl/Ge(111), Phys. Rev. B **93**, 085412 (2016).

[10] E. Annese, T. Kuzumaki, B. Müller, Y. Yamamoto, H. Nakano, H. Kato, A. Araki, M. Ohtaka, T. Aoki, H. Ishikawa, T. Hayashida, J. R. Osiecki, K. Miyamoto, Y. Takeichi, A. Harasawa, K. Yaji, T. Shirasawa, K.-I. Nittoh, W. Yang, K. Miki *et al.*, Nonvortical Rashba spin structure on a surface with C_1h symmetry, Phys. Rev. Lett. **117**, 016803 (2016).

[11] T. Kobayashi, Y. Toichi, K. Yaji, Y. Nakata, Y. Yaoita, M. Iwaoka, M. Koga, Y. Zhang, J. Fujii, S. Ono, Y. Sassa, Y. Yoshida, Y. Hasegawa, F. Komori, S. Shin, S. Ichinokura, R. Akiyama, S. Hasegawa, T. Shishidou, M. Weinert *et al.*, Revealing the hidden spin-polarized bands in a superconducting Tl bilayer crystal, Nano Lett. **23**, 7675 (2023).

[12] P. Härtl, S. Schemmelmann, P. Krüger, M. Donath, and M. Bode, Structural and electronic properties of Tl films on Ag(111): From $(\sqrt{3}\times\sqrt{3})$ surface alloy to moiré superstructure, Phys. Rev. B **107**, 205144 (2023).

[13] S. N. P. Wissing, K. T. Ritter, P. Krüger, A. B. Schmidt, and M. Donath, Spin-dependent size of interband hybridization gap: The interplay of adlayer and substrate states in Pb/Cu(111), Phys. Rev. B **91**, 201403(R) (2015).

[14] T. Fauster, Quantization of electronic states on metal surfaces, Appl. Phys. A **59**, 479 (1994).

[15] P. M. Echenique and J. B. Pendry, Theory of image states at metal surfaces, Prog. Surf. Sci. **32**, 111 (1989).

[16] F. Passek and M. Donath, Spin-split image-potential-induced surface state on Ni(111), Phys. Rev. Lett. **69**, 1101 (1992).

[17] A. B. Schmidt, M. Pickel, M. Wiemhöfer, M. Donath, and M. Weinelt, Spin-dependent electron dynamics in front of a ferromagnetic surface, Phys. Rev. Lett. **95**, 107402 (2005).

[18] M. Donath, C. Math, M. Pickel, A. B. Schmidt, and M. Weinelt, Realization of a spin-polarized two-dimensional electron gas via image-potential-induced surface states, Surf. Sci. **601**, 5701 (2007).

[19] S. Tognolini, S. Achilli, L. Longetti, E. Fava, C. Mariani, M. I. Trioni, and S. Pagliara, Rashba spin-orbit coupling in image potential states, Phys. Rev. Lett. **115**, 046801 (2015).

[20] T. Nakazawa, N. Takagi, M. Kawai, H. Ishida, and R. Arafune, Rashba splitting in an image potential state investigated by circular dichroism two-photon photoemission spectroscopy, Phys. Rev. B **94**, 115412 (2016).

[21] F. Schöttke, S. Schemmelmann, P. Krüger, and M. Donath, Rashba-split image-potential state and unoccupied surface electronic structure of Re(0001), Phys. Rev. B **105**, 155419 (2022).

[22] V. Dose, Momentum-resolved inverse photoemission, Surf. Sci. Rep. **5**, 337 (1985).

[23] M. Donath, Spin-dependent electronic structure at magnetic surfaces: The low-Miller-index surfaces of nickel, Surf. Sci. Rep. **20**, 251 (1994).

[24] S. D. Stolwijk, H. Wortelen, A. B. Schmidt, and M. Donath, Rotatable spin-polarized electron source for inverse-photoemission experiments, Rev. Sci. Instrum. **85**, 013306 (2014).

[25] A. Zumbülte, A. B. Schmidt, and M. Donath, Momentum resolution in inverse photoemission, Rev. Sci. Instrum. **86**, 013908 (2015).

[26] C. Thiede, I. Niehues, A. B. Schmidt, and M. Donath, The acetone bandpass detector for inverse photoemission: Operation in proportional and Geiger–Müller modes, Meas. Sci. Technol. **29**, 065901 (2018).

[27] J. P. Perdew and A. Zunger, Self-interaction correction to density-functional approximations for many-electron systems, Phys. Rev. B **23**, 5048 (1981).

[28] B. Stärk, P. Krüger, and J. Pollmann, Magnetic anisotropy of thin Co and Ni films on diamond surfaces, Phys. Rev. B **84**, 195316 (2011).

[29] L. Kleinman and D. M. Bylander, Efficacious form for model pseudopotentials, Phys. Rev. Lett. **48**, 1425 (1982).

[30] L. A. Hemstreet, C. Y. Fong, and J. S. Nelson, First-principles calculations of spin-orbit splittings in solids using nonlocal separable pseudopotentials, Phys. Rev. B **47**, 4238 (1993).

[31] L. Eschmann, A. Sabitova, R. Temirov, F. S. Tautz, P. Krüger, and M. Rohlfing, Coverage-dependent anisotropy of the NTCDA/Ag(111) interface state dispersion, Phys. Rev. B **100**, 125155 (2019).

[32] R. O. Jones, P. J. Jennings, and O. Jepsen, Surface barrier in metals: A new model with application to W(001), Phys. Rev. B **29**, 6474 (1984).

[33] In the simple model, the order of the spin-split states for B is not altered by altering the position of the Tl atoms.

[34] The spectral shape of an image-potential state appears as a peak from the $n = 1$ state of the Rydberg-like series plus a step-like increase due to the higher members of the series plus continuum states above the vacuum level (see Fig. 1 in Ref. [38])

[35] D. Straub and F. J. Himpsel, Spectroscopy of image-potential states with inverse photoemission, Phys. Rev. B **33**, 2256 (1986).

[36] K. Giesen, F. Hage, F. J. Himpsel, H. J. Riess, W. Steinmann, and N. V. Smith, Effective mass of image-potential states, Phys. Rev. B **35**, 975 (1987).

[37] In Fig. 4(a), the peak positions were determined by a fitting procedure due to the more complex background intensity around the image states, which influences the peak positions. In (c), where the signal-to-background intensity is high for all states, the peak positions were extracted by eye.

[38] W. von der Linden, M. Donath, and V. Dose, Unbiased access to exchange splitting of magnetic bands using the maximum entropy method, Phys. Rev. Lett. **71**, 899 (1993).